An Analysis of a Transformerless Dual Active Half-Bridge Converter

Research paper

Robert Sosnowski, Maciej Chojowski*[iD], Marcin Baszyński[iD]

AGH University of Science and Technology, Kraków, Poland

Abstract: This paper proposes a transformerless dual half-bridge converter (TLDAHB). By eliminating the transformer and harnessing the possibility of using a low inductor value, it is possible to minimise the size of the converter. A phase-shift pulse width modulation will result in a wide controlled voltage gain of the converter and operation as buck and boost. The theoretical topology analysis, simulation, and experimental results are presented. Theoretical analysis consists of analysis of power transfer and design. In case of experimental research, particular attention was paid to power transfer and efficiency analysis. Near zero switching transient of voltage in the half-bridge topology results with high efficiency.

Keywords: DC-DC converter • bidirectional converter • phase-shift control • zero voltage transient

1. Introduction

The cascade connection of the buck and boost topology is a simple one that is used in applications where voltage reduction, as well as voltage increase, is required. An example may be the application of such a system to photovoltaics (PV) panels that have been oversized; and at the peak of the generated energy, there is a need to limit the voltage of the inverter (Chang et al., 2018). Another example is the power factor correction (PFC) system, which also has a buck-boost system for voltage regulation on the DC side (Badawy et al., 2016). The topologies (Badawy et al., 2016; Chang et al., 2017) are simply a combination of buck and boost circuits. Control is achieved by modulating the pulse width. There are studies looking for other topologies with higher efficiency by using zero current switching (ZCS) and zero voltage switching (ZVS) as well as control methods of systems (Alonso et al., 2011; Fernão Pires et al., 2018). Such systems can be one-way or two-way and multi-phase, as in Bereš et al. (2017). The availability of multiple phases makes it possible to reduce passive elements and output voltage fluctuations (Bereš et al., 2017). Systems for targeted applications allow, for example, to reduce the number of power switches and optimise the entire device (Alonso et al., 2011; Fernão Pires et al., 2018). The circuits (Alonso et al., 2011; Chang et al., 2017, 2018; Fernão Pires et al., 2018) do not have galvanic isolation, which can be provided by the dual active bridge (DAB) (Tong et al., 2018). The DAB circuit achieves high efficiency and can achieve soft switching (Everts et al., 2014; Karshenas et al., 2011; Tong et al., 2018) within the appropriate range. The DAB system differs from other systems (Alonso et al., 2011; Chang et al., 2017, 2018; Fernão Pires et al., 2018) in that it controls the phase shift of pulse-width modulation (PWM) signals (Tong et al., 2018; Wu et al., 2016). The circuit shown in Amin et al. (2015) is called a transformerless DAB circuit. Shift control is possible by using a capacitor to block the DC component. It also has a bidirectional seven energy capability, such as DAB (Everts et al., 2014) or a buck-boost circuit (Zhu and Maksimović, 2021). The arrangement also allows for a soft rebate and creates a loss (Kasper et al., 2016).

The article contains an extended analytical description and simulation results of a prototype converter from the system (Amin et al., 2015). Laboratory tests were carried out with about 15 times greater power and 50 times higher output voltage than in Amin et al. (2015). The converter power has been drastically increased to meet the power needs of the electronic application. Theoretical formulas describing the TLDAHB system were analysed and confirmed by the experimental setup.

* Email: chojo@agh.edu.pl

The remainder of this paper is organised as follows. Section 2 presents the theoretical aspects of the TLDAHB DC-DC converter. Section 3 contains the results of the laboratory tests of the proposed system. The waveforms of the voltages and the input current are presented in Section 4. An efficiency test for a variable phase-shift control has been included. Moreover, the possibilities of the output voltage control and power transfer have been tested and compared with the theoretical equations. Section 5 concludes the article.

2. Topology Analysis

The proposed converter of the TLDAHB converter is presented in Figure 1. The converter does not provide isolation (no transformer), but there is one common ground – the input and output ground are connected together.

The topology has two half-bridge converters and an *LC* branch. The capacitor *C* is used only as a DC isolation capacitor and the converter operating frequency f_S far above resonant frequency f_0:

$$f_S \gg f_0 = \frac{1}{2\pi\sqrt{LC}} \tag{1}$$

The symmetrical topology allows the transfer of energy to both sides with variable voltage gain, which is an advance of the converter.

2.1. Power transfer of the TLDAHB

Phase shift enables an easy power transfer to take place in the converter, and the theoretical operation for the same has been presented in Figure 2. The PWM signal for input and output half bridges are shifted by the angle φ. The different voltage levels corresponding to the shift cause the current to flow through the choke and transfer the power (Figure 2). The shift value can be determined in time domain:

$$T_\varphi = \varphi \frac{T_S}{2\pi} \wedge T_S = \frac{1}{f_S} \tag{2}$$

where T_S is the switching period.

The voltage of LC branch $(u_{LC}(t) = u_L(t) + u_C(t))$ in stage I is equal to the input voltage. In stage II, $u_{LC}(t)$ is equal to the difference between input and output voltages. In stage III, $u_{LC}(t)$ is equal to minus output voltage, while in stage IV, it is equal to zero. The mean value of $u_{LC}(t)$ is equal to half of the difference between input and output voltages.

For the properly selected capacitor, $u_C(t)$ is almost constant and equal to the mean value of $u_{LC}(t)$. The variable component of $u_{LC}(t)$ is approximately equal to voltage of inductor $(u_L(t))$.

As a consequence, if the input voltage is smaller than the output voltage (buck operation), this implies that the current in stage II is decreasing; and if the input voltage is greater than the output voltage (boost operation), this implies that the current in stage II is increasing.

The averaged output current for a resistive load *R* is described by:

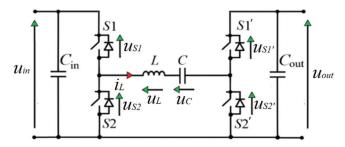$$I_{out} = \frac{U_{out}}{R} = \frac{U_{in}}{8\pi^2 L f_S} \varphi\left(\pi - |\varphi|\right) \tag{3}$$

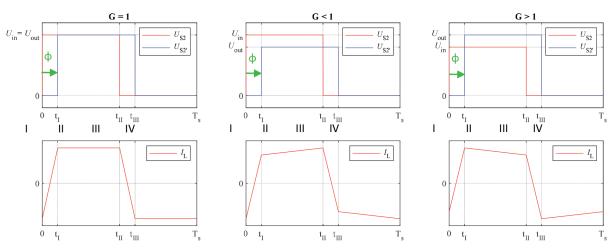**Fig. 1.** The general concept of TLDAHB. TLDAHB, transformerless dual half-bridge converter.

Fig. 2. The general concept of phase-shift control – TLDAHB operation. TLDAHB, transformerless dual half-bridge converter.

The identical shape of the current of the described system and the DAB system produces the result that the output method is the same as for the commonly known DAB converter (Alonso et al., 2011; Chang et al., 2017, 2018; Fernão Pires et al., 2018). Power transfer of the converter is (Amin et al., 2015):

$$P_{TLDAB} = I_{out}U_{out} = \frac{U_{in}U_{out}}{8\pi^2 L f_S} \varphi(\pi - |\varphi|) \tag{4}$$

where U_{in} and U_{out} are DC input and output voltages, respectively, and L is an induction of main inductor. Eq. (4) is maximal, when:

$$\frac{dP_{TLDAB}}{d\varphi} = 0 \tag{5}$$

and

$$|P_{max}| = \frac{dP_{TLDAB}}{d\varphi} = \pi \frac{U_{in}U_{out}}{8\pi^2 L f_S} - 2|\varphi|\frac{U_{in}U_{out}}{8\pi^2 L f_S} = 0 \tag{6}$$

Therefore, when $\varphi = \pm\frac{\pi}{2}$, the power is:

$$|P_{max}|_{\varphi=\pm\frac{\pi}{2}} = \frac{1}{32}\frac{U_{in}U_{out}}{L f_S} \tag{7}$$

A normalised power transfer may be defined as:

$$P_N = \frac{p_{TLDAB}(\varphi)}{|P_{max}|} = \frac{4}{\pi^2}\varphi(\pi - |\varphi|) \tag{8}$$

The power transfer function has a part that is similar to dual active bridge $\varphi(\pi - |\varphi|)$ (Tong et al., 2018). The advantage of a dual active bridge is that the transformer turns ratio, which can be useful for example in high boosting application.

The voltage gain G is given by:

$$G = \frac{U_{out}}{U_{in}} = R\frac{\varphi(\pi - |\varphi|)}{8\pi^2 L f_S} \tag{9}$$

where R represents the resistance of the load.

2.2. Design of the TLDAHB

During the design process, the induction L value needed to transfer the maximum power P_{max} (for averaged voltage levels U_{in} and U_{out} and switching frequency f_S) is given as:

$$L = \frac{1}{32} \frac{U_{in} U_{out}}{P_{max} f_S} \tag{10}$$

The theoretical voltage stress for the transistor in the input half bridge is:

$$U_{S1} = U_{S2} = U_{in} \tag{11}$$

And for the output bridge:

$$U_{S1'} = U_{S2'} = U_{out} \tag{12}$$

Isolating capacitor voltage is almost constant (only small ripple during operation) and can be calculated by:

$$U_C = \frac{1}{2}\left(U_{in} - U_{out}\right) \tag{13}$$

The soft switching in the first half-bridge with transistors S1 and S2 is ensured when the following formula stands satisfied:

$$\varphi_{H1} \geq \frac{\pi}{2}\left(\frac{U_{out} - U_{in}}{U_{out}}\right) \tag{14}$$

For the second half bridge it is necessary to satisfy (Amin et al., 2015):

$$\varphi_{H2} \geq \frac{\pi}{2}\left(\frac{U_{in} - U_{out}}{U_{in}}\right) \tag{15}$$

To obtain soft switching, it is also required to allow time to recharge the output capacitance of the transistor C_{oss} and the minimum dead time value can be calculated by:

$$t_{dead} \approx \frac{\pi}{4}\sqrt{LC_{oss}} \tag{16}$$

Selecting the inductor and transistors require determining root mean square (RMS) values of currents. The choke current is described by:

$$i_L(t) = \begin{cases} i_1(t) = \dfrac{I_1 - I_0}{T_\varphi}t + I_0 & for \ \ 0 \leq t \leq T_\varphi \\[2mm] i_2(t) = \dfrac{-I_0 - I_1}{\frac{T_s}{2} - T_\varphi}\left(t - T_\varphi\right) + I_m & for \ T_\varphi \leq t \leq \dfrac{T_s}{2} \\[2mm] i_3(t) = -i_1\left(t - \dfrac{T_s}{2}\right) & for \ \ \dfrac{T}{2} \leq t \leq \dfrac{T_s}{2} + T_\varphi \\[2mm] i_4(t) = -i_2\left(t - \dfrac{T_s}{2}\right) & for \ \ \dfrac{T_s}{2} + t_\varphi \leq t \leq T_s \end{cases} \tag{17}$$

where

$$I_0 = i_L(0) = \frac{\pi\left(U_{out} - U_{in}\right) - 2\varphi U_{out}}{8\pi L f_s} \wedge I_1 = i_L\left(T_\varphi\right) \tag{18}$$

To determine I_1 It can be used to determine the mean value of the input current, which is described by:

$$I_{in\,av} = \frac{1}{T_s}\int_0^{T_s} i_{in}(t)\,dt = \frac{1}{T}\left(\int_0^{T_\varphi} i_1(t)\,dt + \int_{T_\varphi}^{\frac{T_s}{2}} i_2(t)\,dt\right) =$$

$$= \frac{1}{T_s}\left(\int_0^{T_\varphi}\left(\frac{I_1-I_0}{T_\varphi}t + I_0\right)dt + \int_{T_\varphi}^{\frac{T_s}{2}}\left(\frac{-I_0-I_1}{\frac{T_s}{2}-T_\varphi}(t-T_\varphi)+I_1\right)dt\right) =$$

$$= \frac{1}{T_s}\left(\int_0^{T_\varphi}\left(\frac{I_1-I_0}{T_\varphi}t + I_0\right)dt + \int_0^{\frac{T_s}{2}-T_\varphi}\left(\frac{-I_0-I_1}{\frac{T_s}{2}-T_\varphi}t + I_1\right)dt\right) =$$

$$= \frac{1}{T_s}\left[\frac{1}{2}(I_1-I_0)T_\varphi + I_0 T_\varphi + \left[\frac{1}{2}(-I_0-I_1)+I_1\right]\left(\frac{T_s}{2}-T_\varphi\right)\right] = \frac{1}{4}I_1 + I_0\left(\frac{T_\varphi}{T_s}-\frac{1}{4}\right)$$

(19)

Using Eq. (2), the following formula can be obtained:

$$I_{in\,av} = \frac{1}{4}I_1 + I_0\left(\frac{\varphi}{2\pi}-\frac{1}{4}\right)$$

(20)

If $\eta = \dfrac{P_{out}}{P_{in}} = 1$, then $U_{out}I_{out} = U_{in}I_{in\,av}$, so $I_{in\,av}$ is described by:

$$I_{in\,av} = \frac{U_{out}I_{out}}{U_{in}} = \frac{U_{out}^2}{U_{in}R} = \frac{(GU_{in})^2}{U_{in}R} = \frac{G^2 U_{in}}{R}$$

(21)

Using Eqs (20) and (21), the following equation can be obtained:

$$\frac{1}{4}I_1 + I_0\left(\frac{\varphi}{2\pi}-\frac{1}{4}\right) = \frac{G^2 U_{in}}{R}$$

(22)

Transforming Eq. (22), the following formula can be obtained:

$$I_1 = 4\left[\frac{G^2 U_{in}}{R} - I_0\left(\frac{\varphi}{2\pi}-\frac{1}{4}\right)\right]$$

(23)

The RMS value of the choke current is described by:

$$I_{L\,rms} = \sqrt{\frac{1}{T_s}\int_0^{T_s} i_L^2(t)\,dt} = \sqrt{\frac{1}{T}\left(\int_0^{t_\varphi} i_1^2(t)\,dt + \int_{t_\varphi}^{\frac{T_s}{2}} i_2^2(t)\,dt + \int_{\frac{T}{2}}^{\frac{T_s}{2}+t_\varphi} i_3^2(t)\,dt + \int_{\frac{T_s}{2}+t_\varphi}^{T_s} i_4^2(t)\,dt\right)}$$

$$= \sqrt{\frac{1}{T_s}(A+B+C+D)}$$

(24)

Using Eq. (17), the value of component A is described by:

$$A = \int_0^{t_\varphi} i_1^2(t)\, dt = \int_0^{t_\varphi} \left(\frac{I_1 - I_0}{t_\varphi} t + I_0 \right)^2 dt = \int_0^{t_\varphi} \left[\left(\frac{I_1 - I_0}{t_\varphi} \right)^2 t^2 + 2\frac{I_1 - I_0}{t_\varphi} I_0 t + I_0{}^2 \right] dt =$$

$$= \frac{1}{3}\left(\frac{I_1 - I_0}{t_\varphi} \right)^2 t_\varphi{}^3 + \frac{I_1 - I_0}{t_\varphi} I_0 t_\varphi{}^2 + I_0{}^2 t_\varphi = t_\varphi \left[\frac{1}{3}(I_1 - I_0)^2 + (I_1 - I_0)I_0 + I_0{}^2 \right] =$$

$$= \frac{1}{3} t_\varphi \left(I_1^2 + I_1 I_0 + I_0^2 \right)$$

(25)

Using Eq. (2), the following formula can be obtained:

$$A = \frac{\varphi T_s}{6\pi}\left(I_1^2 + I_1 I_0 + I_0^2 \right)$$

(26)

Using Eq. (17), the value of component B is described by:

$$B = \int_{t_\varphi}^{\frac{T_s}{2}} i_2^2(t)\, dt = \int_{t_\varphi}^{\frac{T_s}{2}} \left(\frac{-I_0 - I_1}{\frac{T_s}{2} - t_\varphi}(t - t_\varphi) + I_1 \right)^2 dt = \int_0^{\frac{T_s}{2} - t_\varphi} \left(\frac{-I_0 - I_1}{\frac{T_s}{2} - t_\varphi} t + I_1 \right)^2 dt =$$

$$= \int_0^{\frac{T_s}{2} - t_\varphi} \left[\left(\frac{-I_0 - I_1}{\frac{T_s}{2} - t_\varphi} \right)^2 t^2 + 2 I_1 \frac{-I_0 - I_1}{\frac{T_s}{2} - t_\varphi} t + I_1^2 \right] dt = \left(\frac{T_s}{2} - t_\varphi \right)\left[\frac{1}{3}(-I_0 - I_1)^2 - I_0 I_1 \right] =$$

(27)

$$= \frac{1}{3}\left(\frac{T_s}{2} - t_\varphi \right)\left(I_0^2 - I_0 I_1 + I_1^2 \right)$$

Using Eq. (2), the following equation can be obtained:

$$B = \frac{1}{3}\left(\frac{T_s}{2} - \frac{\varphi T_s}{2\pi} \right)\left(I_0^2 - I_0 I_1 + I_1^2 \right) = \frac{T_s}{6}\left(1 - \frac{\varphi}{\pi} \right)\left(I_0^2 - I_0 I_1 + I_1^2 \right)$$

(28)

Based on Eq. (17), the values of components C and D are described by:

$$C = \int_{\frac{T_s}{2}}^{\frac{T_s}{2} + t_\varphi} i_3^2(t)\, dt = A$$

(29)

$$D = \int_{\frac{T_s}{2} + t_\varphi}^{T_s} i_4^2(t)\, dt = B$$

(30)

Using Eqs (26)–(30), the RMS value of the choke current is described by:

$$I_{L\,rms} = \sqrt{\frac{1}{T_s}(A + B + C + D)} = \sqrt{\frac{2}{T_s}(A + B)} = \sqrt{\frac{\varphi}{3\pi}\left(I_1^2 + I_1 I_0 + I_0^2 \right) + \left(\frac{1}{3} - \frac{\varphi}{3\pi} \right)\left(I_0^2 - I_0 I_1 + I_1^2 \right)} =$$

$$= \sqrt{\frac{1}{3}\left[I_0^2 + \left(\frac{2\varphi}{\pi} - 1 \right) I_0 I_1 + I_1^2 \right]}$$

(31)

The RMS value of the transistor current is described by:

$$I_{T\,rms} = \sqrt{\frac{1}{T_s}(A+B)} = \frac{I_{L\,rms}}{\sqrt{2}} \qquad (32)$$

2.3. Simulation results

The results in Figure 3 show only the steady state operation simulation of the TLDAHB system (simulation parameters are listed in Table 1). The simulation results confirmed (Figure 3) that all transistors have a similar RMS
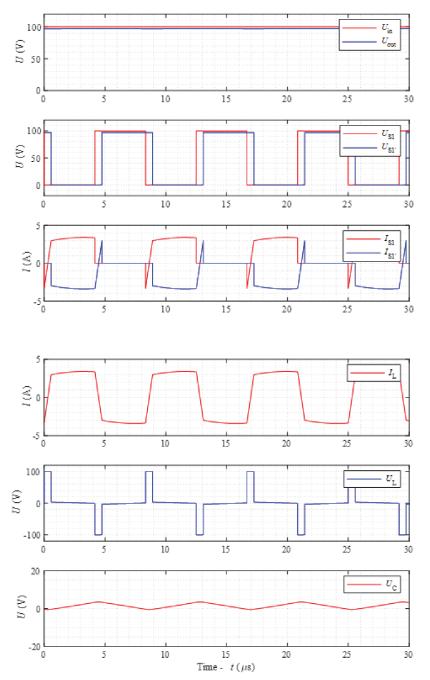

Fig. 3. Waveforms of voltages (input, output, inductor, and capacitor) and currents (inductor and transistors) of proposed converter operation.

current value, the voltage across the transistors T1 and T2 is equal to the input voltage, and the voltage across the transistors T1′ and T2′ is equal to the output voltage. The simulation results obtained are approximately consistent with the theoretical runs. The current waveforms differ to some extent from the expected ones because of the inconsistency of the elements (e.g. the conduction resistance of transistors).

3. Experimental Results

3.1. Practical circuit realisation of the TLDAHB

The experimental TLDAHB system was developed to test the converter operation and confirm the theoretical considerations discussed in Section 2. The circuit was tested in order to check the principle of operation, the concept of achieving voltage control over the outputs by shifting between bridges, voltage gain, and efficiency. Table 2 lists important parameters of the converter and control modulation. Transistors and DC capacitors are mounted on two printed circuit boards (PCBs). The configuration is optimised not to demonstrate volumetric power density but to obtain reliable performance and enable system verification.

3.2. Operation of the TLDAHB

To verify the basic concept of the converter (Figure 1), the open loop phase-shift control has been tested. The laboratory setup is presented in Figure 4.

The experimental waveforms presented in Figures 5–8 confirm that the converter operates according to the discussed theoretical pattern. Figures 5–7 show operation with voltage gain lower than G < 1 (buck operation). The voltages on the inductor and DC blocking capacitor are shown in Figure 5. The voltage ripple (the peak-to-peak value) on the DC blocking capacitor is <4.5 V. Further increasing the capacity will reduce the fluctuations. Additionally, in Figure 6, the overshoot during transient voltage is clearly seen. In Figure 7, with slightly higher power transfer, the transistor soft switching occurs (ZVS). The converter can also operate as boosting topology, which is confirmed in Figure 8 (G > 1).

Parameter	Value
Input voltage U_{in}	100 V
Angle φ	25º
Load resistance R_{load}	68 Ω
Output capacitor C_{out}	200 μF
Resonant and operating frequency	f_0 = 29.35 kHz, fs = 120 kHz
DC blocking capacitor C	3.2 μF
Inductor L	L = 9.19 μH, R_{ESR} = 118.81 mΩ
Transistors $S1, S2, S1′, S2'$	$R_{DS(on)}$ = 60 mΩ
Dead time	100 ns

Table 1. Simulation parameters.

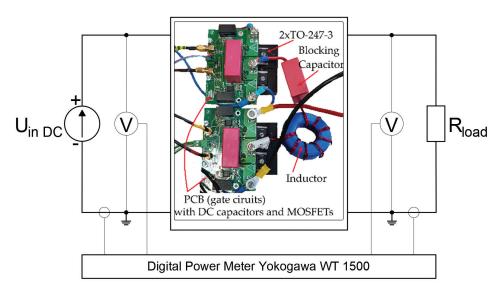| Parameter	Value
Input voltage U_{in} and power P_{max}	100 V and 400 W
Input capacitor C_{in}	2 × 4.7 μF ± 10% + 1. μF ± 5%
Output capacitor C_{out}	2 × 100 μF ± 10% + 1. μF ± 5%
Resonant and operating frequency	f_0 = 29.35 kHz, fs = 120 kHz
DC blocking capacitor C	3.2 μF ± 10% (~650 V)
Inductor L	SENDUS (MS-226060) 8 turns, (L = 9.19 μH, R_{ESR} = 118.81 mΩ for 120 kHz)
Transistors $S1, S2, S1′, S2′$	SiCMOSFET – C3M0060065D ($V_{DS(on)}$ = 650 V, $R_{DS(on)}$ = 60 mΩ, I_D = 29 A)
Dead time	100 ns

Table 2. Experimental setup.

Fig. 4. Experimental setup of the voltage, current, and power metre – power transfer, efficiency, and voltage gain measurement.
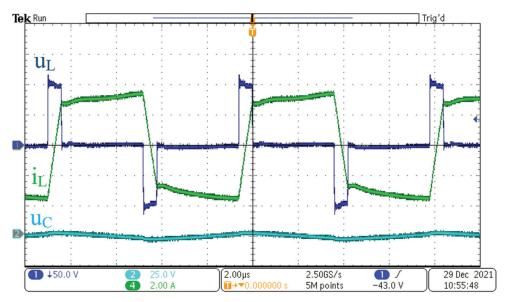

Fig. 5. Experimental waveforms of TLDAHB. CH1, inductor voltage u_L; CH2, capacitor voltage u_C; CH4, i_L inductor current; TLDAHB, transformerless dual half-bridge converter.

3.3. Comparison of the experimental results with simulation results and theoretical analysis

The parameters of the experimental setup for Figure 5 are approximately the same as for the simulation (Figure 3).

The gain value for experimental results is designated based on the $u_C(t)$ waveform. Theoretical values are those determined by Eqs (9), (13), (18), and (23) (Table 3).

The obtained results can be considered consistent with each other. Differences between obtained values are relatively small. One of the main reasons for these differences is the assumption of 100% efficiency for theoretical analysis. Another reason is variability of elements' parameters, e.g. inductance of inductor L.

3.4. Efficiency and power transfer of the converter

The efficiency and power transfer function have been measured using a Yokogawa WT 1500 power analyser, which, for DC power measurements, has an accuracy equal to the sum of 0.1% of the reading and
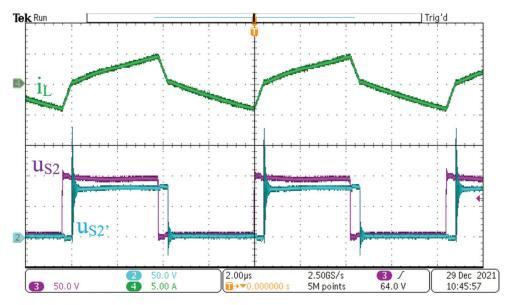
Fig. 6. Experimental waveforms of TLDAHB. CH2, drain-source transistor $u_{S2'}$ voltage; CH3, drain-source transistor u_{S2} voltage; CH4, i_L inductor; blocking capacitor current, $P_{in} \approx 110$ W; output voltage, $U_{out} \approx 86$ V; no ZVS, the overshoot in $u_{S2'}$ transistor voltage during turn off; TLDAHB, transformerless dual half-bridge converter.
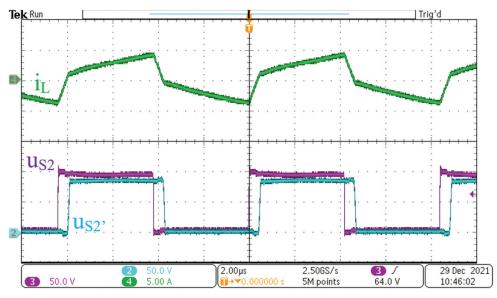

Fig. 7. Experimental waveforms of TLDAHB. CH2, drain-source transistor $u_{S2'}$ voltage; CH3, drain-source transistor u_{S2} voltage; CH4, i_L inductor; blocking capacitor current, $P_{in} \approx 115$ W; output voltage, $U_{out} \approx 88$ V with ZVS for second half-bridge; TLDAHB, transformerless dual half-bridge converter.

0.1% of the range values (YOKOGAWA, 2019). The power transfer has been visualised in Figure 9, with theoretical transferred power based on Eq. (2). The phase-shift angle has been reduced to 50° (which corresponds to 350 W). The voltage gain is presented in Figure 10, with a fitted theoretical function based on Eq. (6).

The maximal achieved value of the efficiency (Figure 11) is given by η = 98.5% (for R = 94 Ω, $P \approx 90$ Ω, and f_s = 120 kHz). Based on the gain and efficiency curves, it can be stated that the system can be especially applied when there is a need to change the voltage in a relational small range ($0.8 < G < 1.2$).
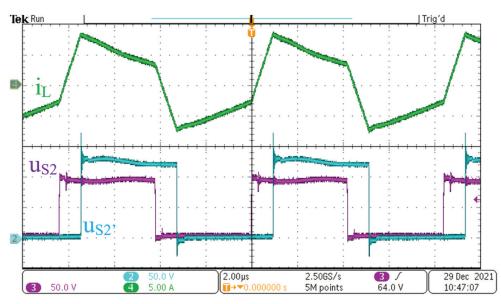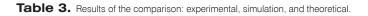
Fig. 8. Experimental waveforms of TLDAHB. CH2, drain-source transistor $u_{S2'}$ voltage; CH3, drain-source transistor u_{S2} voltage; CH4, iL inductor; blocking capacitor current, operation in the boosting mode $U_{in} < U_{out}$; TLDAHB, transformerless dual half-bridge converter.

Parameter	Experimental (Figure 5)	Simulation (Figure 3)	Theoretical (Eqs (9), (13), (18), and (23))
G [-]	0.96	0.96	0.92
U_c [V]	2	2	4
I_0 [A]	−3.5	−3.3	−3.8
I_1 [A]	2.7	3.0	2.3

Table 3. Results of the comparison: experimental, simulation, and theoretical.
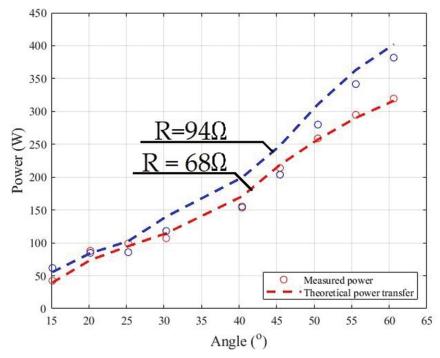

Fig. 9. Measured power transfer (with theoretical curve based on Eq. [4]) of the converter versus shift angle at constant frequency $f_S = 120$ kHz.
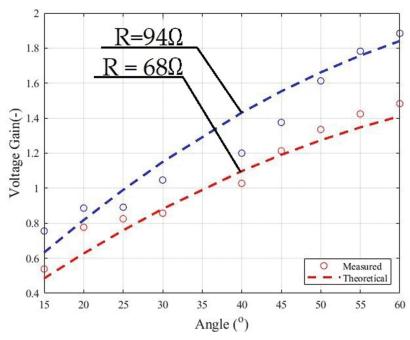
Fig. 10. Measured voltage gain (with theoretical curve based on Eq. [9]) of the converter versus shift angle at constant frequency f_s = 120 kHz.
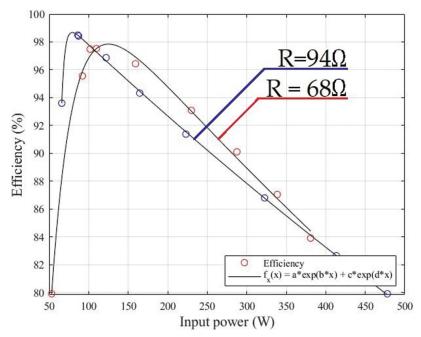

Fig. 11. Measured efficiency (with approximation curve) of the converter versus input power at operating frequency f_s = 120 kHz without an external airflow.

4. Conclusions

This paper presents a concept of the topology and confirmed practical results of the DC-DC converter. The most important topology advantage is transformerless and low inductor value needed. These features enable minimalization of the overall size of the converter.

The paper (Subsection 3.3) presents a comparison of parameters determined experimentally, using simulation and based on theoretical equations. The results obtained using these methods are approximately equal.

Moreover, the paper presents the measured and theoretical power transfer and voltage gain curves (versus shift angle at constant frequency). The measured and theoretical values can be considered consistent with each other (Subsection 3.4). The confirmation of the theoretical power transfer is considered a novel aspect.

The presented results confirm also the possibility of buck-boost operation with the continuous output voltage regulation with phase shift (like classic isolated dual active bridge).

Furthermore, this paper confirms the possibility of ZVS operation (Figure 7) in a specific phase-shift range, which improves the efficiency. The highest obtained efficiency value (using SiC MOSFETs) is 98.5%.

Acknowledgements

References

Alonso, J. M., Vina, J., Vaquero, D. G., Martinez, G. and Osorio, R. (2011). Analysis and Design of the Integrated Double Buck–Boost Converter as a High-Power-Factor Driver for Power-LED Lamps. *IEEE Transactions on Industrial Electronics*, 59(4), pp. 1689–1697. doi: 10.1109/TIE.2011.2109342.

Amin, A., Shousha, M., Prodić, A. and Lynch, B. (2015). A transformerless dual active half-bridge DC-DC converter for point-of-load power supplies. In: *2015 IEEE Energy Conversion Congress and Exposition (ECCE)*, 2015, 133–140. doi: 10.1109/ECCE.2015.7309680.

Badawy, M. O., Sozer, Y. and De Abreu-Garcia, J. A. (2016). A Novel Control for a Cascaded Buck–Boost PFC Converter Operating in Discontinuous Capacitor Voltage Mode. *IEEE Transactions on Industrial Electronics*, 63(7), pp. 4198–4210. doi: 10.1109/TIE.2016.2539247.

Bereš, M., Schweiner, D., Kováčová, I. and Kalinov, A. (2017). Current ripple comparison of multi and single phase buck-boost converters. In: *2017 International Conference on Modern Electrical and Energy Systems (MEES)*, 2017, 260–263. doi: 10.1109/MEES.2017.8248905.

Chang, C H., Cheng, C A. and Cheng, H L. (2017). A bidirectional buck-cascaded buck-boost PV inverter with active power filtering. In: *IEEE 6th Global Conference on Consumer Electronics (GCCE)*, 2017, 1–4. doi: 10.1109/GCCE.2017.8229357.

Chang, C. H., Cheng, C A. and Cheng, H L. (2018). An interleaved buck-cascaded buck-boost inverter for PV grid-connection applications. In: *2018 International Power Electronics Conference (IPEC-Niigata 2018 -ECCE Asia)*, 2860–2865. doi: 10.23919/IPEC.2018.8507516.

Everts, J., Krismer, F., Van den Keybus, J., Driesen, J. and Kolar, J. W. (2014). Optimal ZVS Modulation of Single-Phase Single-Stage Bidirectional DAB AC–DC Converters. *IEEE Transactions on Power Electronics*, 29(8), pp. 3954–3970. doi: 10.1109/TPEL.2013.2292026.

Fernão Pires, V., Foito, D., Cordeiro, A. and Silva, J. F. (2018). A single-switch DC/DC buck-boost converter with extended output voltage. In: *2018 7th International Conference on Renewable Energy Research and Applications (ICRERA)*, 2018, 791–796. doi: 10.1109/ICRERA.2018.8566996.

Kasper, M., Burkart, R. M., Deboy, G. and Kolar, J. W. (2016). ZVS of Power MOSFETs Revisited. *IEEE Transactions on Power Electronics*, 31(12), pp. 8063–8067. doi: 10.1109/TPEL.2016.2574998.

Karshenas, H. R., Daneshpajooh, H., Safaee, A., Jain, P. K. and Bakhshai, A. (2011). *Bidirectional DC – DC Converters for Energy Storage Systems*. doi: 10.5772/23494.

Tong, A., Hang, L., Li, G., Jiang, X. and Gao, S. (2018). Modeling and Analysis of a Dual-Active-Bridge-Isolated Bidirectional DC/DC Converter to Minimize RMS Current with Whole Operating Range. *IEEE Transactions on Power Electronics*, 33(6), pp. 5302–5316. doi: 10.1109/TPEL.2017.2692276.

Wu, H., Mu, T., Ge, H. and Xing, Y. (2016). Full-Range Soft-Switching-Isolated Buck-Boost Converters with Integrated Interleaved Boost Converter and Phase-Shifted Control. *IEEE Transactions on Power Electronics*, 31(2), pp. 987–999. doi: 10.1109/TPEL.2015.2425956.

YOKOGAWA. (2019). WT500 Power Analyzer. WT500 Power Analyzer Datasheet. [online] Available at: https://tmi.yokogawa.com/solutions/products/power-analyzers/ [Accessed 2 May 2021].

Zhu, J. and Maksimović, D. (2021). Transformerless Stacked Active Bridge Converters: Analysis, Properties, and Synthesis. *IEEE Transactions on Power Electronics*, 36(7), pp. 7914–7926. doi: 10.1109/TPEL.2020.3042748.